machines

MDPI

Article

Numerical and Experimental Investigation of the Ultra-Low Head Bidirectional Shaft Extension Pump Under Near-Zero Head Conditions

Fulin Zhang [1,*], Yuan Zheng [2], Gaohui Li [1] and Jing Dai [2]

[1] PowerChina Huadong Engineering Corporation Limited, Hangzhou 311122, China
[2] College of Water Conservancy and Hydropower Engineering, Hohai University, Nanjing 210098, China
* Correspondence: zhang_fl2@hdec.com

Abstract: Theoretical analysis, numerical simulation, and experimental study are used to investigate the ultra-low head bidirectional shaft extension pump, especially near-zero head conditions. The results show that under forward operation, at low flow and design flow conditions, the closer to the shroud, the closer the vortex is to the back of the guide vanes, and the vortex area is becoming smaller. The hydraulic loss of the outlet passage is 15% of the operating head at the minimum flow and 170% of the operating head under near-zero head condition. The peak-to-peak (PTP) value of pressure fluctuation increases with the increase in flow rate. The primary frequency (PF) of vibration is strongly related to the primary and secondary frequencies (PSFs) of pressure fluctuation. Under reverse operation, when the flow rate is less than $0.83Q_{r0}$, the uniformity of axial velocity distribution V_u and the velocity-weighted average angle θ show an approximately exponential declining pattern. The hydraulic loss of the outlet passage at the minimum flow rate is 61% of the operating head and 350% of the operating head under near-zero head condition. The exponential fitting can better describe the relationship between circulation and hydraulic loss. As the flow rate decreases, the PF of vibration decreases to rotational frequency.

Keywords: shaft extension pump; bidirectional operation; near-zero head; fluid–structure interaction; pressure fluctuation; vibration

check for updates

Academic Editor: Konstantinos Kyprianidis

Received: 10 February 2025
Revised: 5 March 2025
Accepted: 6 March 2025
Published: 7 March 2025

Citation: Zhang, F.; Zheng, Y.; Li, G.; Dai, J. Numerical and Experimental Investigation of the Ultra-Low Head Bidirectional Shaft Extension Pump Under Near-Zero Head Conditions. *Machines* **2025**, *13*, 220. https://doi.org/10.3390/machines13030220

Copyright: © 2025 by the authors. Licensee MDPI, Basel, Switzerland. This article is an open access article distributed under the terms and conditions of the Creative Commons Attribution (CC BY) license (https://creativecommons.org/licenses/by/4.0/).

1. Introduction

Horizontal shaft extension pumps are widely used in large and medium-sized low head pumping stations. Its main advantage is that it has better hydraulic performance under low head, while the structure is simple, easy to install and maintain, requires less investment, and provides a good working environment for the motor [1]. However, due to the low operating head, especially under start-up and shutdown operation, it frequently operates at near-zero head conditions with a large flow rate, posing a significant threat to the device's stability. And for drainage and irrigation requirements, many pumping stations require two-way operation. But the airfoil of the guide vane is in the anti-arch state under reverse operation, and the guide vane will generate a positive pre-whirl, resulting in the performance and cavitation characteristic dropping significantly. The turbulent flow inside the flow passages causes noise and vibration, making the project a serious safety hazard.

First, to obtain a more complete understanding of the performance, it is essential to study the flow field within the pump. Goltz et al. [2] experimentally investigated the clearance vortex and the endwall flow field in axial-flow pumps running into stall and the

extent to which these flow phenomena influence the pump characteristic as well as the overall pump vibrations. Li et al. [3] investigated the flow characteristics and performance of an axial-flow pump with an inducer. Zhang et al. [4] simulated the pressure fluctuation with k-ε RNG turbulence model and SIMPLEC algorithm and carried out the experimental investigation for the adjustable pump. Prasad et al. [5] carried out a shear stress transport (SST) k-ω turbulence model at different guide vane opening and rotational speeds of an experimentally tested model of an axial-flow turbine. Kan et al. [6] studied the internal flow of an axial-flow pump at design condition and stall conditions using computational fluid dynamics (CFD) technology and a prototype pressure fluctuation test. Yang et al. [7], based on the CFD, investigated the flow characteristics and optimized the flow passage by analyzing the state of the vortex in vertical submersible pump under a two-way operation.

The fluid–structure interaction (FSI) is a significant and complicated phenomenon which is the prime cause of excessive vibrations in many pumps. Pozarlik and Benra et al. [8,9] compared two-way and one-way coupling methods for numerical analysis of FSI, and the results show that the one-way interaction can be a useful approximation in the prediction of the amplitude and vibration pattern of the structure. Lerche et al. [10] used a one-way FSI method to determine blade stresses on a centrifugal compressor. Birajdar et al. [11] simulated the FSI of a vertical turbine pump using the one-way coupling method to predict the flow-induced vibrations on different components. Shi et al. [12] adopted the unidirectional FSI method to analyze the pressure distribution and deformation distribution of a full tubular pump under different conditions.

Cavitation is a critical physical phenomenon in pumps, leading to performance degradation. Zhang et al. [13,14] used CFD and high-speed photography to investigate the trajectory of the tip leakage vortex (TLV) and tip leakage flow characteristics in an axial-flow pump. Hong et al. [15] developed a new transport-equation-based cavitation model, validated it through experimental results, then studied the mechanism of TLV cavitation with this model.

The fluid excitation force generated by the unsteady flow in the pump device is one of the main sources for vibration, and the physical phenomena contained in the flow-induced vibration process are very complex. Also, the pressure fluctuation is also one of the main causes of vibration. Wang et al. [16] studied the pressure fluctuation at the inlet and outlet of an impeller and guide vane in an axial-flow pump at different working conditions. Ma et al. [17] computed and analyzed the pressure fluctuation of a bidirectional pump at flow passage, blade surfaces, and guide vane surfaces. Xie et al. [18] established the relationship between internal pressure fluctuation, which was obtained from the numerical calculation of prototype and model devices under different working conditions. Shervani-Tabar et al. [19] developed a methodology to monitor the performance of an axial-flow pump under cavitation based on fault diagnosis strategies.

At present, a lot of research has been carried out on the shaft extension pump, and many results have been obtained. However, the relationship between the flow characteristics and hydraulic loss, cavitation, pressure fluctuation, vibration, as well as the FSI of bidirectional shaft extension pump, especially at near-zero head, has not been studied systematically and thoroughly. This paper conducts a comprehensive study on the flow characteristics, hydraulic loss, FSI, cavitation, pressure fluctuation, and vibration characteristics of the bidirectional shaft extension pump, combined with a theoretical analysis, to establish the relationship between internal and external characteristics, so as to provide a reference for the safe and stable operation of pumping systems.

2. Numerical Simulation and Experimental Setup

2.1. Governing Equations and Cavitation Model

The continuity and momentum equations for the incompressible flow are as follows:

$$\frac{\partial \rho}{\partial t} + \frac{\partial}{\partial x_i}(\rho \overline{u}_i) = 0 \tag{1}$$

$$\frac{\partial}{\partial t}(\rho \overline{u}_i) + \frac{\partial}{\partial x_j}(\rho \overline{u}_i \overline{u}_j) = -\frac{\partial \overline{p}}{\partial x_i} + \frac{\partial}{\partial x_j}(\mu \frac{\partial \overline{u}_i}{\partial x_j} - \rho \overline{u}_i' \overline{u}_j') \tag{2}$$

where $\overline{u}$, $\overline{p}$, ρ, and μ are the mean velocity, the mean pressure, the fluid density, and the fluid dynamic viscosity, respectively. In order to solve the "closure problem", it is necessary to model the Reynolds stress tensor. According to the Boussinesq assumption, the Reynolds stress tensor can be described as follows:

$$-\overline{u}_i' \overline{u}_j' = -v_t(\frac{\partial \overline{u}_i}{\partial x_j} + \frac{\partial \overline{u}_j}{\partial x_i}) + \frac{2}{3}\delta_{ij}k \tag{3}$$

where v_t and k are the eddy viscosity and the turbulent kinetic energy, respectively.

$$k = -\frac{1}{2}\overline{u}_i' \overline{u}_j' \tag{4}$$

The SST k-ω model was developed by Menter [20], adopting the k-ω model in the near wall region and the k-ε model in the far field. In order to balance the computational time and accuracy, the SST k-ω model was used for computation. The k and ω equations can be described as follows:

$$\frac{\partial}{\partial t}(\rho k) + \frac{\partial}{\partial x_i}(\rho k u_i) = \frac{\partial}{\partial x_j}(\Gamma_k \frac{\partial k}{\partial x_j}) + G_k - Y_k \tag{5}$$

$$\frac{\partial}{\partial t}(\rho \omega) + \frac{\partial}{\partial x_i}(\rho \omega u_i) = \frac{\partial}{\partial x_j}(\Gamma_\omega \frac{\partial \omega}{\partial x_j}) + G_\omega + D_\omega - Y_\omega \tag{6}$$

where G_k and G_ω are the source terms of the turbulent kinetic energy (k) and dissipation rate (ω), respectively; Y_k and Y_ω are the dissipation terms of k and ω, respectively; D_ω is the diffusion term of ω; and Γ_k and Γ_ω are the effective diffusion coefficients of k and ω, respectively.

The cavitation is modeled by the vapor volume fraction mass transfer equation:

$$\frac{\partial}{\partial t}(\alpha_v \rho_v) + \frac{\partial}{\partial x_j}(\alpha_v \rho_v u_j) = \dot{m}^+ - \dot{m}^- \tag{7}$$

where α_v and ρ_v are the volume fraction and density of vapor, respectively; $\dot{m}^+$ and $\dot{m}^-$ represent the cavitation source terms, the evaporation and condensation, respectively. $\dot{m}^+$ and $\dot{m}^-$ are given by the following:

$$\dot{m}^+ = C_e \frac{3\rho_v(1-\alpha_v)\alpha_{nuc}}{R_b}\sqrt{\frac{2(p_v - p)}{3\rho_l}}(p \le p_v) \tag{8}$$

$$\dot{m}^- = C_c \frac{3\rho_v \alpha_v}{R_b}\sqrt{\frac{2(p - p_v)}{3\rho_l}}(p \ge p_v) \tag{9}$$

where C_e and C_c are empirical coefficients for the different phase change processes; α_{nuc} is the nucleation site volume fraction; R_b is the typical bubble size in water; p and p_v are the local static pressure and saturated vapor pressure, respectively; ρ_l is the density of the liquid.

The coefficients are set as follows: $C_e = 50$, $C_c = 0.01$, $\alpha_{nuc} = 5 \times 10^{-4}$, $R_b = 1 \times 10^{-6}$ m, and $p_v = 3540$ Pa [21,22].

The governing equations for the structural model are given by the following equation of motion:

$$M\ddot{q}(t) + C\dot{q}(t) + Kq(t) = Q(t) \quad (10)$$

where M, C, and K are the structural mass matrix, the structural damping matrix and the structural stiffness matrix, respectively; $\ddot{q}(t)$, $\dot{q}(t)$, and $q(t)$ represent a nodal acceleration vector, a nodal velocity vector, and a nodal displacement vector, respectively; $Q(t)$ is the applied load vector, which is responsible for linking the unsteady aerodynamics and inertial loads with the structural dynamics. The blade pressures from the fluid are included here.

2.2. Computational Domain, Mesh, and Numerical Setup

Figure 1 shows the fluid computational domain of a pump model that is composed of an inlet passage, impeller, rotor, guide vane, and outlet passage. The pump consists of a 4-blade impeller and a 5-blade guide vane (stator). The diameter of the impeller D_1 is 300 mm. The tip clearance size h is 0.3 mm, and the rotation speed n is 906.67 r/min. The flow rate at the design point are as follows: under a forward operation, the flow rate $Q_{f\,0}$ is 196 kg/s; under a reverse operation, the flow rate Q_{r0} is 178 kg/s; the superscript 0, f, and r stand for the design point, forward operation, and reverse operation, respectively.

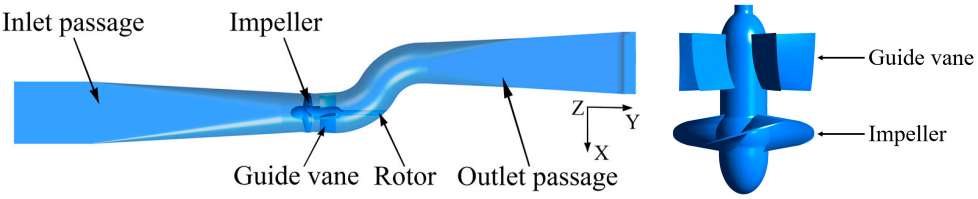


Figure 1. Fluid computational domain of pump model.

The mesh is critical to the accuracy and efficiency of the computation and affects the validity and reliability of the computation results. The structured hexahedral mesh of the inlet passage and outlet passage are generated via ANSYS-ICEM 17.0 software. The meshing of the impeller and guide vane are carried out using the ANSYS-TurboGrid 17.0 software. Figure 2 shows the structured mesh of the impeller and guide vane. As shown in Figure 3, y^+ on the blade surface varied from 0.1 to 60.2, which is suitable for the SST k-ω model with high R_e in the tip region flow.

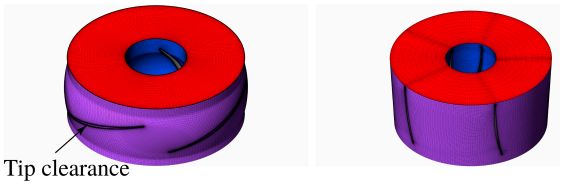


Figure 2. Mesh of impeller (**left**) and guide vane (**right**).

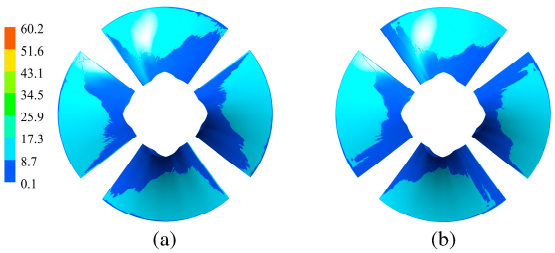


Figure 3. Distribution of y^+ on surface of blades: (**a**) pressure side (PS) and (**b**) suction side (SS).

As shown in Figure 4, when the total number of grids for the computational domain is more than 5.93×10^6, the relative error of the computation result of head is less than 1%. To balance the computational accuracy and computational load, the mesh with 5.93×10^6 grid was adopted.

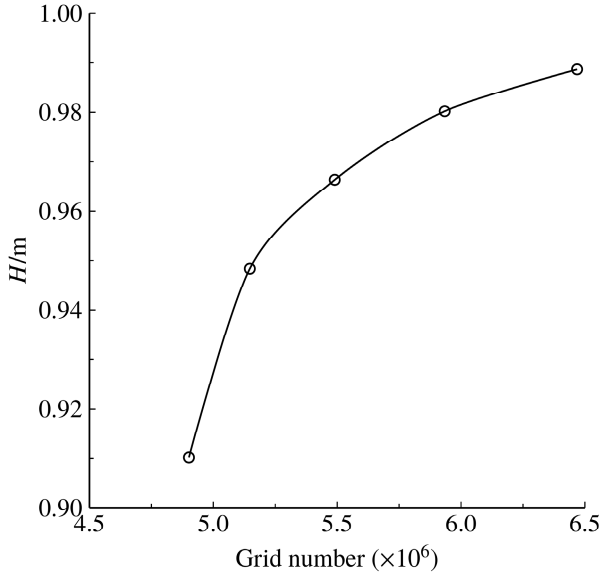


Figure 4. Grid independence check.

In this study, the ANSYS-CFX 17.0 is used for the fluid field calculation. For boundary conditions, a constant mass flow rate and flow direction are given at the inlet. At the outlet, the average static pressure is imposed. All surfaces of the pump are no-slip wall boundary conditions. The computational domains are discretized by the element-based finite volume method and performed using a high-resolution scheme for the convection and diffusion terms. The "frozen rotor" model is chosen for the interfaces between the rotor and stator. The convergence criterion is 10^{-4} in the simulation [23].

In the computation with cavitation, the model for vapor/liquid two-phase flows assumes that the fluid is homogeneous. The mass transfers caused by cavitation between the liquid and vapor are described by the Rayleigh–Plesset equations [24].

The structural part has been solved with structure dynamics methods using ANSYS-Mechanical code. The FSI coupling utilized is a one-way coupling. The structural code then solves the displacements and stresses. The material of the structure is the structural steel with the theoretical density of 7850 kg/m^3, the Young's modulus is 200 GPa, the yield strength is 550 MPa, and the Poisson's ratio is 0.3. The structural part is divided into tetrahedral grids in ANSYS-Mechanical, which contains 799,963 nodes and 251,839 elements. The mesh study is performed and shown in Table 1. When the total number of nodes is more than 799,963, the relative error of the maximum stress is less than 2%.

Table 1. Mesh study for the structural part.

Nodes	Elements	Maximum Stress (MPa)
1,328,790	408,440	21.314
799,963	251,839	20.947
447,851	144,995	20.118
316,158	107,761	18.837
247,435	83,375	17.364

Figure 5 shows the structural part's constraints. A fixed constraint is applied to the hub surface to prevent the structure from generating rigid body displacement. Cylindrical constraints are adopted on the cylindrical surfaces to constrain the motion in the radial direction. The fluid solid interface transfers data between the fluid and structure domains. In addition, the gravitational acceleration g is set to 9.8066 m/s^2 [12].

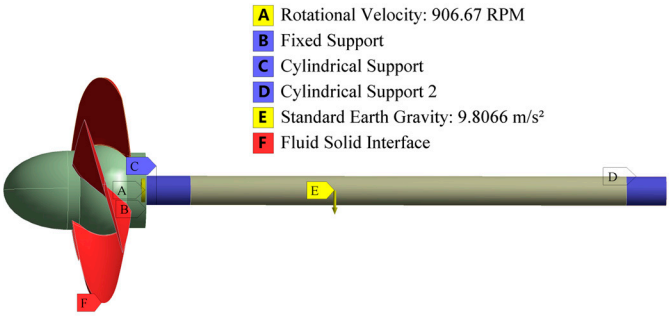
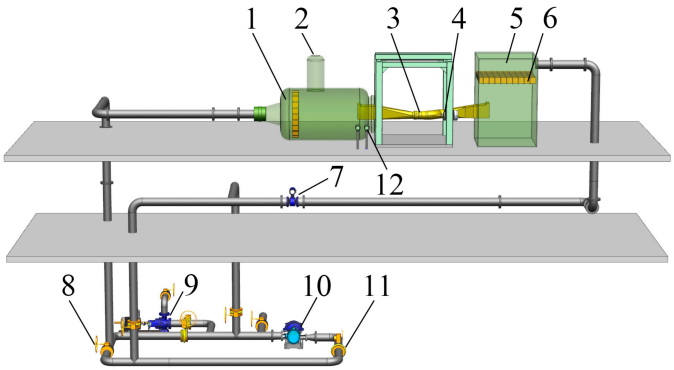


Figure 5. Constraints of the structural part.

2.3. Experimental Setup

Figure 6 shows the model pump test apparatus at the Hohai University, Nanjing, China. The comprehensive error of the test bench is less than 0.39%.



1. Tail tank 2. Cavitation tank 3. Model pump
4. Torque meter and motor 5. Pressure tank 6. Rectifier grid
7. Electromagnetic flow meter 8. Butterfly valve 9. Charge pump
10. Booster pump 11. Electromagnetic valve 12. Pressure gauge

Figure 6. Three-dimensional diagram of the test bench.

A vacuum pump above the tail tank is used to adjust the pressure at the pump inlet at different cavitation number conditions. The storage capacities of the pressure tank and tail tank are 20 m^3 and 12.56 m^3, respectively [25]. The booster pump is used to change the flow rate. The diameter of the impeller is 300 mm, and the casing of the model pump section is made of transparent glass, allowing for the internal flow and cavitation to be visualized. The internal flow and cavitation are imaged by a high-speed digital video camera. The flow rate is measured with an electromagnetic flow meter that is located in a very long and straight pipe. A torque meter is installed to measure the shaft speed and power. The maximum power of the motor is 10 kW. Pressure gauges are installed at the inlet and outlet of the pump to obtain the head.

The layout of the model pump and sensors are shown in Figure 7. Pressure sensors are located at the inlet of the impeller (Point 1) and the outlet of the S-shaped elbow (Point 2) when the pump is running in the forward operation, as shown in Figure 7b. The pressure sensor adopts an HPT700 pressure transmitter; the sampling frequency is 1000 Hz, the

output signal is 4–20 mA, the pressure range is 0–300 kPa, and the accuracy is 0.5%. The vibration sensor is installed between the impeller and guide vane, as shown in Figure 7c. The X direction is the radial direction, the Y direction is the axial direction, and the Z direction is the vertical direction. The vibration sensor adopts the GST three-component piezoelectric acceleration sensor CA-YD-116A, which can measure the vibration in X, Y, and Z directions simultaneously. Its main parameters are as follows: the axial sensitivity is 20 pC/g, the peak measurement range is 1000 g, the frequency response range is 1–6000 Hz, the maximum lateral sensitivity is smaller than 5%, and the magnetic sensitivity is 2 g/T. The collected vibration signal is conditioned using a YE6600 programmable amplifier (developed by Nanjing Anzheng Software Engineering Co., LTD, Nanjing, China) and then enters into the vibration and dynamic signal acquisition and analysis system for processing, which is shown in Figure 7a.

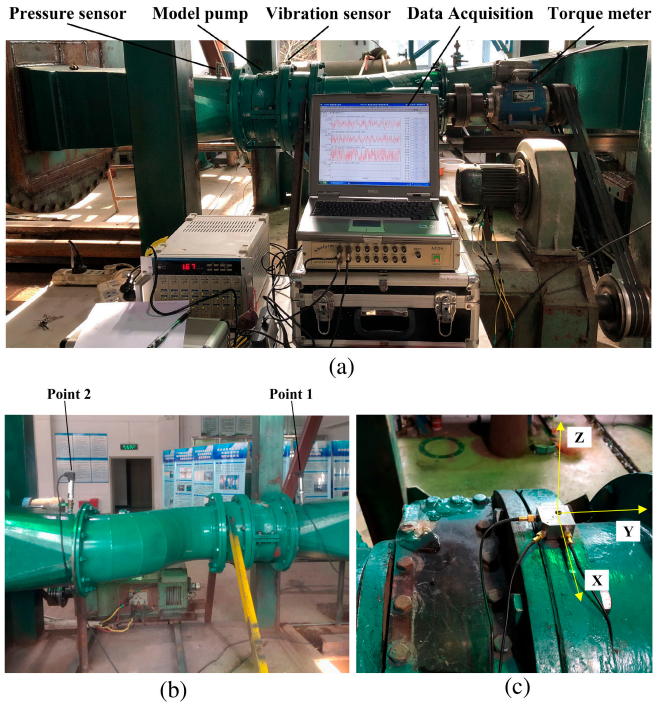


Figure 7. Layout of the model pump and sensors: (**a**) model pump device, (**b**) pressure sensors, (**c**) vibration sensor.

2.4. Validation

Figure 8 shows the head H and the efficiency η with respect to the dimensionless flow rate under forward and reverse operations. From the comparison, we can deduce that the numerical simulation results are consistent with the variation trend in the experimental results. It should be noted that the placement angle of each blade cannot be guaranteed to be exactly the same in the actual installation process, resulting in an inevitable difference between the two. Especially under the low-flow-rate conditions, there are bigger deviations, mainly because the internal flow is more turbulent under the low-flow-rate conditions, which is quite different from the boundary conditions of the numerical simulation. At the same time, due to the obvious turbulence characteristics, the results measured by the experiment have large fluctuations. Overall, the numerical simulation and experimental results demonstrate the same changing trend, and the difference between the two is less than 7%. It is therefore considered that the numerical method can reflect the actual situation qualitatively.

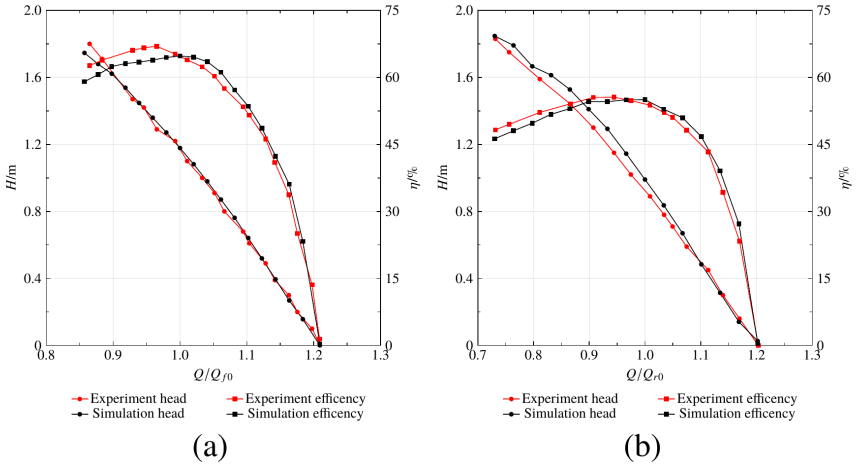


Figure 8. Validation of pump performance: (**a**) forward operation, (**b**) reverse operation.

3. Results and Discussion

The results are analyzed using three flow rates, namely $0.85Q_0$, Q_0, and $1.20Q_0$. In particular, Figure 8 shows that when the flow rate is $1.20Q_0$, the head is near to zero. Under near-zero head conditions, the head produced by the impeller will be dissipated by hydraulic losses in the passages. And the flow rate will be quite large, so the operating condition will be far from optimum, and the efficiency will be very low. As a result, it is critical to analyze the characteristics of near-zero head conditions to prevent damage to the pump.

3.1. Flow Field in the Entire Domain

As shown in Figure 9, when the pump is operating in the forward direction, the flow in the inlet passage is smooth, and the velocity changes evenly. Under low-flow and design-flow conditions, a vortex is formed on the concave side of the S-shaped elbow, and a high-speed zone is formed on the convex side under large-flow conditions. This is determined by the guide vane outlet velocity and the concave–convex structure of the passage at the bend. However, due to the rectification of the guide vane, there is no significant adverse flow inside the outlet passage, and the velocity decreases evenly from inlet to outlet, showing good kinetic energy recovery effect.

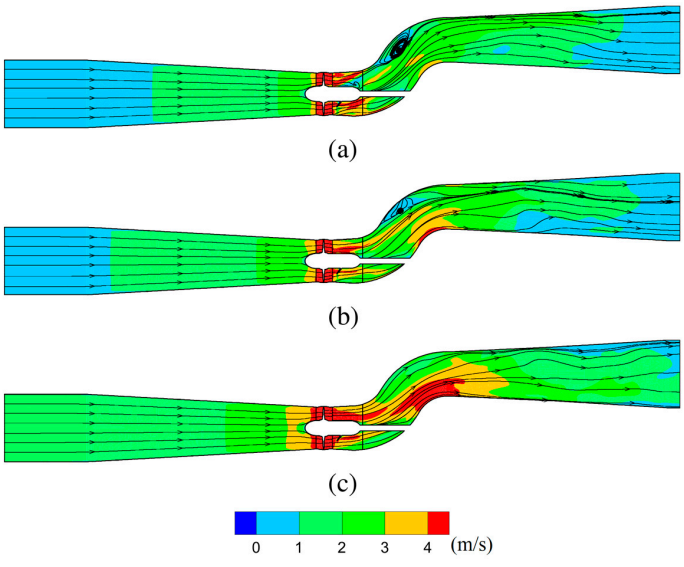


Figure 9. Distribution of velocity magnitude and streamlines under forward operation: (**a**) 0.85 $Q_{f\,0}$, (**b**) $Q_{f\,0}$, (**c**) 1.20 $Q_{f\,0}$.

As shown in Figure 10, due to the lack of rear guide vane, both low-flow and design-flow conditions have severe vortex and backflow inside the outlet passage under the reverse operation. And the vortex grows as the flow rate decreases. Meanwhile, the flow with circulation spirals into the outlet passage and then moves towards the passage's side walls due to centrifugal force, resulting in the flow velocity in the center of the passage being lower. The low-velocity area is irregular under low-flow and design-flow conditions, and the high-velocity area and the low-velocity area alternate, causing the energy gradient to change frequently, and the hydraulic loss in the flow passage also increases.

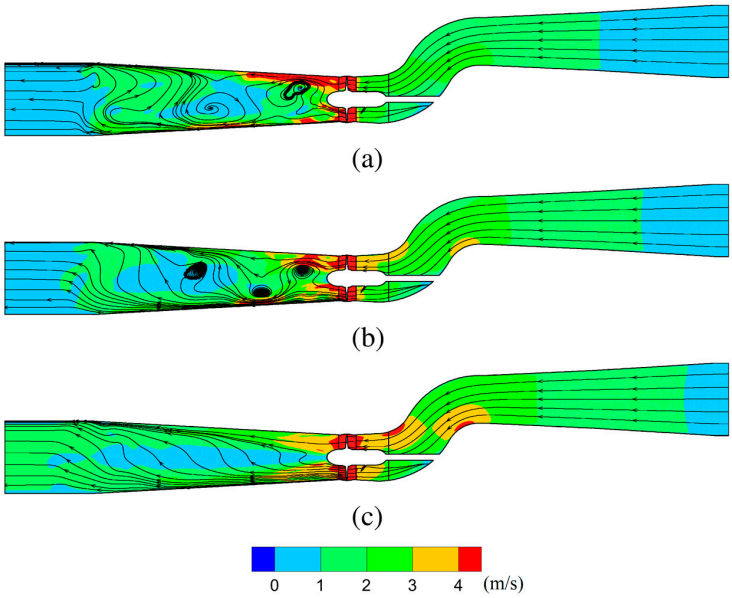


Figure 10. Distribution of velocity magnitude and streamlines under reverse operation: (**a**) 0.85 Q_{r0}, (**b**) Q_{r0}, (**c**) 1.20 Q_{r0}.

3.2. Flow Field Inside the Impeller and Guide Vane

Figure 11 shows the streamlines inside the impeller and guide vanes under forward operation; the locations of surfaces 1, 2, and 3 are demonstrated in Figure 12.

As shown in Figure 11a, under the forward operation, there are obvious vortices on the back of the guide vanes. Under low-flow conditions, the absolute flow angle at the impeller outlet α is smaller than the inlet setting angle of the guide vane β (see Figure 13a). As a result, the water strikes the front of the guide vane, creating vortices on its rear surface. Under large-flow conditions, α is bigger than β (see Figure 13c), and the water hits the back of the guide vanes, resulting in the vortices on the front (see Figure 11c). When the pump is operated at the design point, α should theoretically be equal to β (see Figure 13b), but it is sacrificed to account for the performance under the reverse operation. As a result, the vortices form at the back of the guide vanes (see Figure 11b).

The head generated by the two sections inside and outside the blade must be identical; hence, the closer to the shroud, the smaller the setting angle of the section, as shown in Figure 13d, $\beta_{out} < \beta_{in}$. Therefore, at low-flow and design-flow conditions, the closer the surface to the shroud, the closer the vortex is to the back of the guide vanes, and the vortex area becomes smaller. The vortex gradually disappears as the surface approaches the shroud under large-flow conditions.

The absolute flow angle of the blade inlet edge α_1 can be seen as 90° under forward operation. But under the reverse operation, the α_1 is less than 90°, which is caused by the guide vanes, as shown in Figure 14. As a result, the flow field inside the impeller is more disordered than the forward operation. Moreover, at low-flow conditions, there is obvious flow separation inside the impeller.

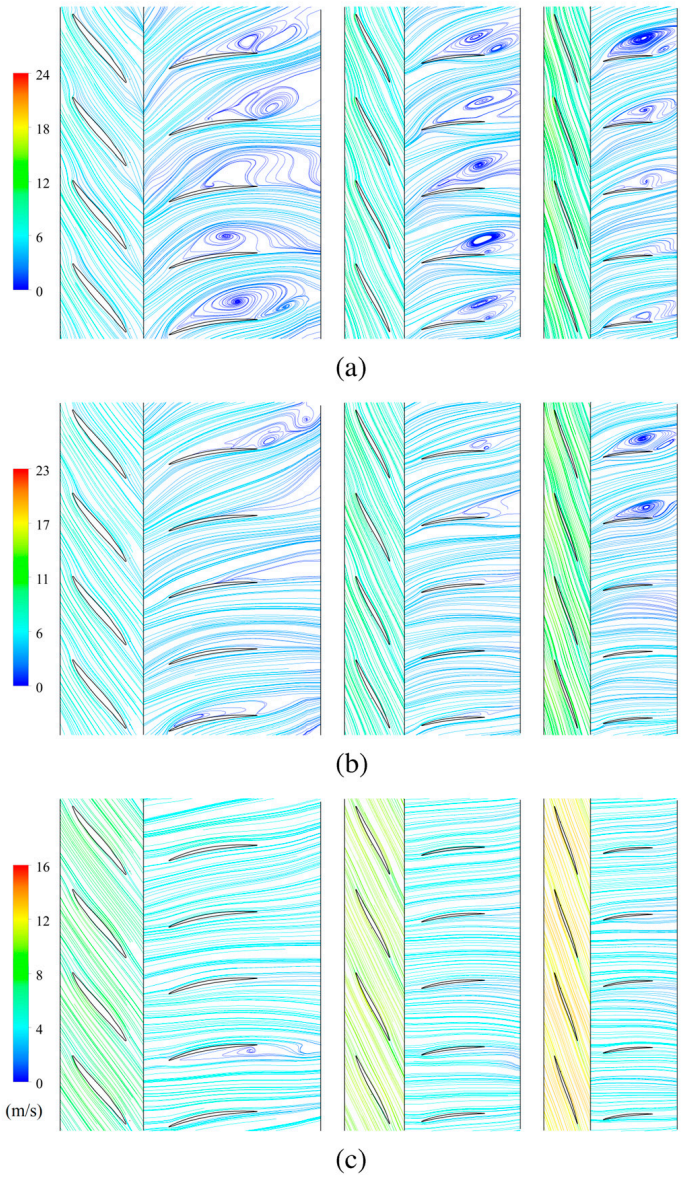


Figure 11. Streamlines inside impeller and guide vanes under forward operation, colored by the velocity magnitude: (**a**) 0.85 $Q_{f\,0}$ (from left to right is surface 1, surface 2, and surface 3, respectively), (**b**) $Q_{f\,0}$, (**c**) 1.20 $Q_{f\,0}$.

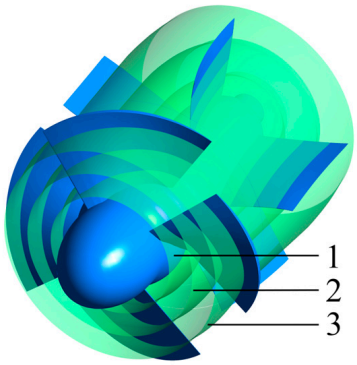


Figure 12. Position of different blade heights: surface 1: span = 0.2, surface 2: span = 0.5, surface 3: span = 0.8.

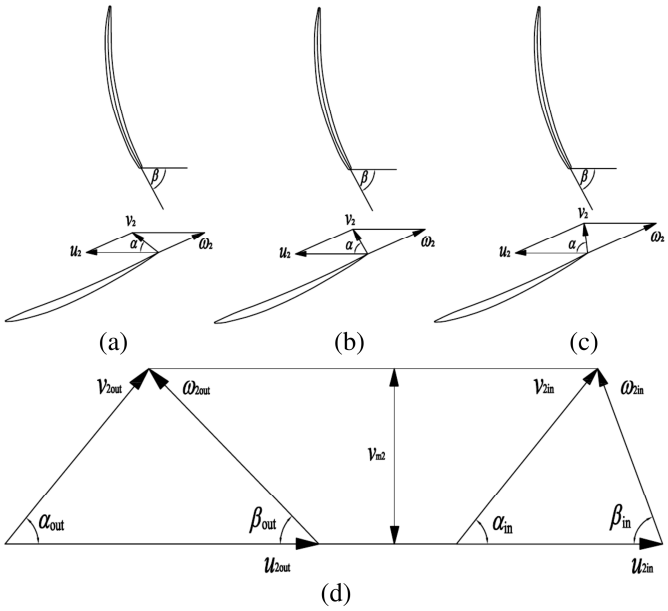


Figure 13. Velocity triangle at the impeller outlet under forward operation: (**a**) Low flow, (**b**) design flow, (**c**) large flow, (**d**) inside and outside sections.

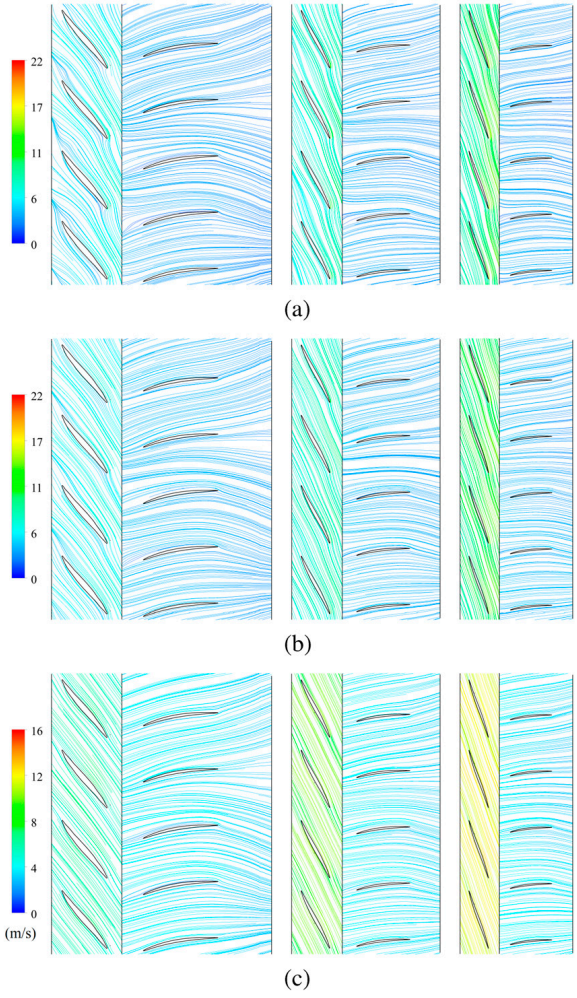


Figure 14. Streamlines inside impeller and guide vanes under reverse operation, colored by velocity magnitude: (**a**) 0.85 Q_{r0} (from **left** to **right** is surface 1, surface 2, and surface 3, respectively); (**b**) Q_{r0}; (**c**) 1.20 Q_{r0}.

It can be found from Figure 15 that because α_1 is less than 90°, V_{u1} is greater than 0, resulting in the declination of lift coefficient. Also, the relative flow angle of the blade inlet edge β_1 becomes bigger, resulting in the optimum operating point leaning towards a lower flow rate under the reverse operation, which can be seen in Figure 8.

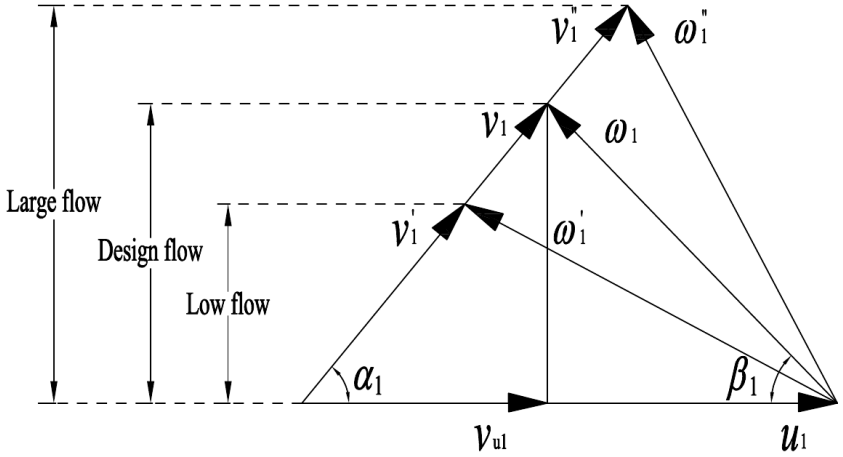


Figure 15. Velocity triangle at the impeller inlet under reverse operation.

Because the positive pre-whirl of the guide vane has a significant influence on the velocity distribution at the impeller inlet under the reverse operation, V_u and θ are introduced for quantitative analysis.

The V_u can be described as follows:

$$V_{\mathrm{u}} = \left\{ 1 - \frac{1}{\overline{U_a}} \sqrt{\left[\sum_{i=1}^{n} (U_{ai} - \overline{U}_a)^2 \right] / n} \right\} \times 100\% \tag{11}$$

where U_a and $\overline{U_{\mathrm{a}}}$ are the axial velocity and the mean axial velocity, respectively; n is the number of elements.

The θ can be described as follows:

$$\theta = \sum_{i=1}^{n} U_{ai} \left[90^\circ - \arctan\left(\frac{U_{ti}}{U_{ai}} \right) \right] / \sum_{i=1}^{n} U_{ai} \tag{12}$$

where U_t is the tangential velocity.

Figure 16 shows V_u and θ under reverse operation. It can be inferred that, at the guide vane inlet, the V_u and θ are independent of the flow rate, the V_u is higher than 83%, and the θ is higher than 89°. At the impeller inlet, θ stabilizes after $0.9Q_{r0}$ and reaches 70°, and the V_u gradually increases with the flow rate and eventually becomes almost the same as the guide vane inlet. Especially, when the flow rate is less than $0.83Q_{r0}$, V_u and θ show an approximately exponential declining pattern, indicating that the front guide vane has a significant negative effect on the flow distribution at the impeller inlet under small flow conditions. As a result, in this model pump, double guide vanes are not used.

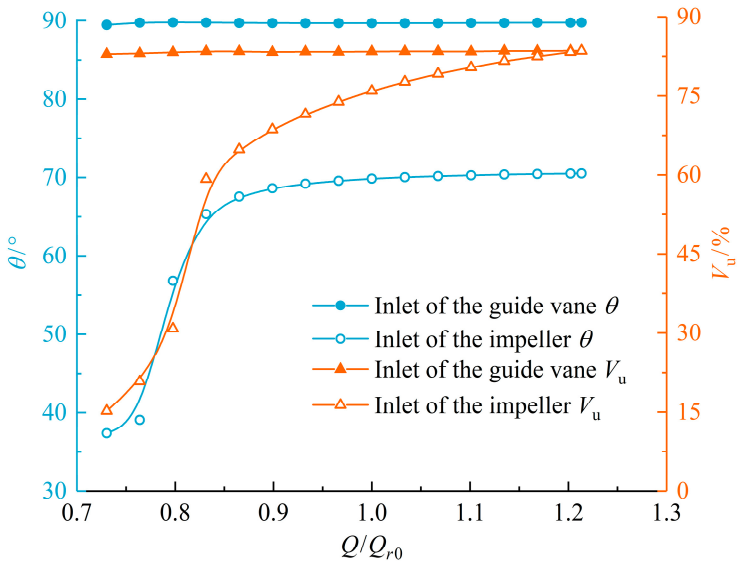


Figure 16. V_u and θ under reverse operation.

3.3. Hydraulic Loss of Flow Passages

The hydraulic loss of the flow passage has a considerable impact on the efficiency of the flow passage and the pump device. The lower the head, the more significant the impact. Figure 17 depicts the hydraulic losses of each part of the outlet passage and the residual kinetic energy at the outlet under forward operation. The hydraulic loss of the S-shaped-bend section is greatest at low flow rates due to the vortex seen in Figure 9 and decreases as the vortex area diminishes. Because of the pipeline loss, the hydraulic loss in the straight pipe section increases progressively as the flow rate increases. For the entire outlet passage, the hydraulic loss reaches the minimum value near the design point. However, it should be noted that the hydraulic loss of the outlet passage at the minimum flow rate is 15% of the operating head and 170% of the operating head under the near-zero head condition. So, under the near-zero head conditions, the energy loss of the pump device is more obvious. The residual kinetic energy at the outlet increases linearly with the increase in flow rate, which also leads to a decrease in the efficiency of the pump unit under near-zero head conditions.

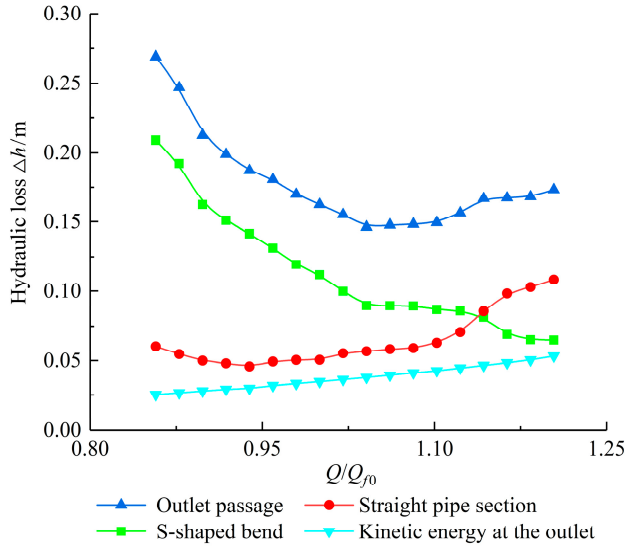


Figure 17. Hydraulic loss and kinetic energy of the outlet under forward operation.

As shown in Figure 18, the hydraulic loss of the inlet passage under reverse operation is only about 10% of that under forward operation, indicating that the flow pattern is turbulent after the high-speed-rotating impeller and guide vane and, at the outlet of the guide vane, still has a residual velocity circulation, resulting in the ratio of the local impact loss and vortex loss accounts for about 90% of the total hydraulic loss of the flow passage. Furthermore, under near-zero head conditions, the hydraulic loss of the inlet passage increases due to the larger flow velocity, and the head is low currently, reducing the device's efficiency significantly.

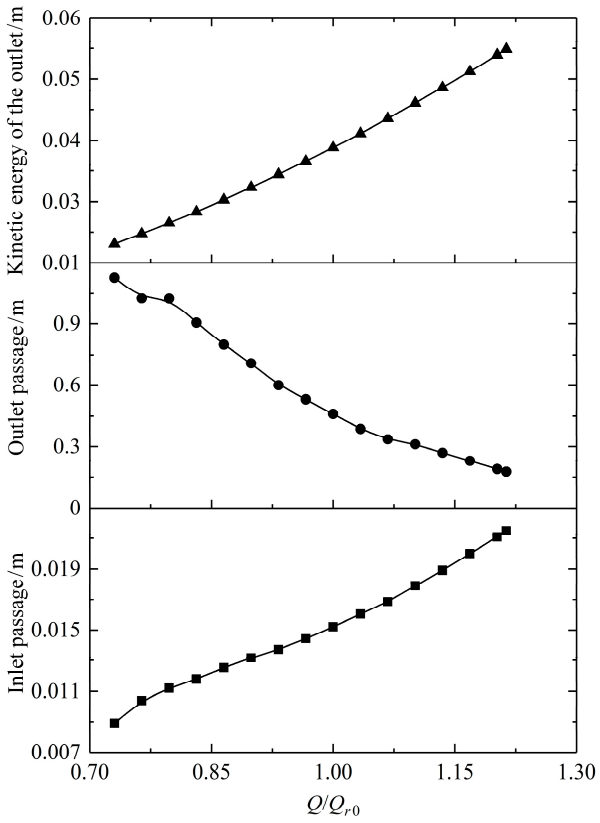


Figure 18. Hydraulic loss and kinetic energy of the outlet under reverse operation.

Rather than being proportional to the square of the flow rate, the hydraulic loss of the outlet passage decreases gradually as the flow rate increases under reverse operation. Because at the impeller outlet has a large residual velocity circulation due to the lack of a rear guide vane, the water spirals into the outlet passage, causing the vortex and backflow shown in Figure 10 [26]. The hydraulic loss of the outlet passage at the minimum flow rate is 61% of the operating head and 350% of the operating head under near-zero head condition. The residual kinetic energy at the outlet is almost the same as that under forward operation.

Compared with the hydraulic loss of the outlet passage under forward operation, the hydraulic loss under reverse operation is several times higher, especially at the minimum flow rate condition, which is 4.2 times. It can be seen from the above analysis that the existence of circulation is the main reason for this gap. To study the relationship between circulation and hydraulic loss, the circulation and hydraulic loss under reverse operation are calculated as shown in Figure 19, where circulation Γ is calculated as follows:

$$\Gamma = \oint_{L_1} v_u dL - \oint_{L_2} v_u dL \tag{13}$$

where L_1 and L_2 are the shroud and hub circumference, respectively; v_u is the circumcomponent of velocity.

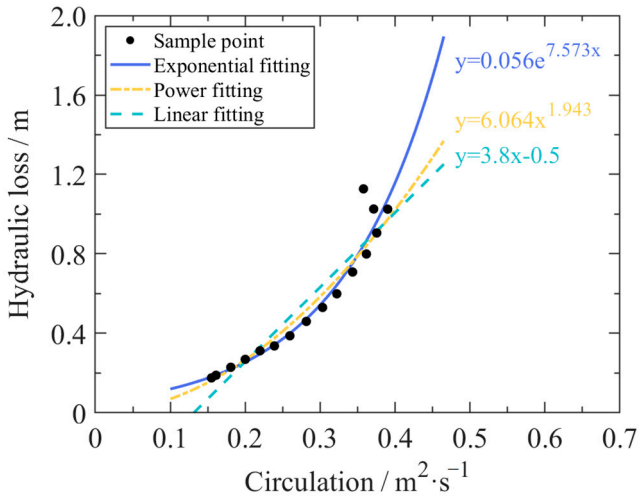


Figure 19. The relationship between the circulation and hydraulic loss of the outlet passage under reverse operation.

From the equation, it can be seen that the circulation increases as the flow rate decreases, because v_u increases at the low-flow-rate conditions, as shown in the velocity triangle in Figure 13. However, near the minimum flow rate, the circulation decreases, as shown in Figure 19. This is because, under the minimum flow rate condition, the water in the boundary layer is hindered and decelerated on the backside of the impeller blades and is separated from the backside of the blades [1]. A backflow zone is formed [27], which reduces the outlet area and increases the relative velocity at the outlet, resulting in a decrease in v_u.

As illustrated in Figure 19, linear, power, and exponential functions are employed to fit the relationship between the circulation and the hydraulic loss of the outlet passage, respectively. The coefficients of determination R^2 for linear, power, and exponential fitting are 0.890, 0.963, and 0.978, respectively. The R^2 of the exponential fitting $y = 0.056e^{7.573x}$ is very close to 1, so the outcomes are thought to be well predicted, and the equation can be utilized for estimating the hydraulic loss of the outlet passage in practical engineering.

3.4. FSI

The equivalent (von-Mises) stress distribution on the PS and SS of the blades are shown in Figures 20 and 21. The equivalent stress decreases first and then increase from the leading edge (LE) to the trailing edge (TE) under both operating directions. The larger equivalent stress appears near the rim of the LE and at the blade root near the LE. The stress concentration is formed because of the huge flow impact generated in the LE, and it is prone to crack and fracture. At the TE near the hub, the equivalent stress increases again. Because the static pressure of the impeller fluid domain increases as the flow rate decreases and the head increases, more intense hydraulic pressures fluctuation will be applied to the surface of the blades, resulting in the maximum equivalent stress of the impeller increases as the flow rate decreases. However, the maximum equivalent stress under all operating conditions is well below the material's yield strength and meets the design requirements.

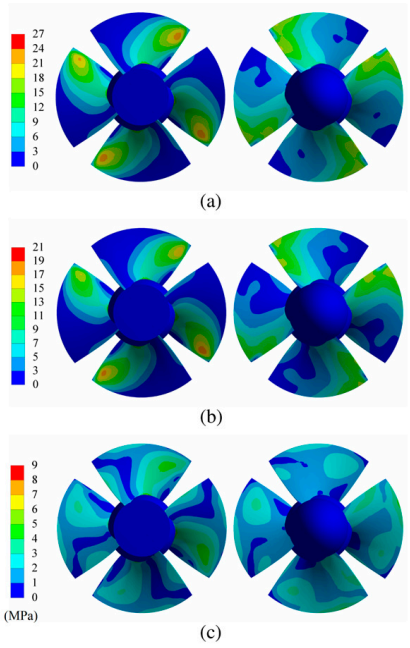


Figure 20. Equivalent (von-Mises) stress of blades under forward operation: (**a**) $0.85Q_{f\,0}$ (from **left** to **right** is PS and SS, respectively), (**b**) $Q_{f\,0}$, (**c**) $1.20Q_{f\,0}$.

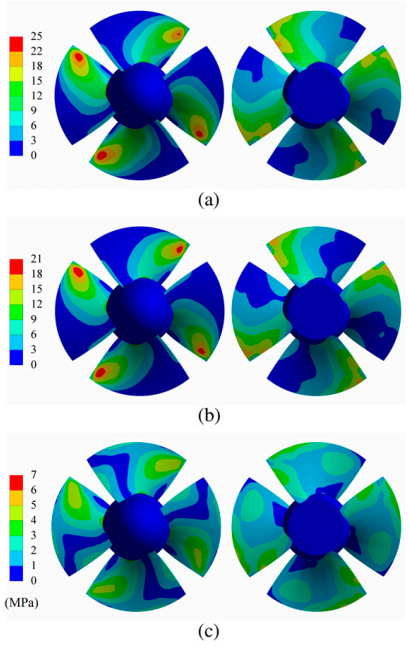


Figure 21. Equivalent (von-Mises) stress of blades under reverse operation: (**a**) $0.85Q_{r0}$ (from **left** to **right** is PS and SS, respectively), (**b**) Q_{r0}, (**c**) $1.20Q_{r0}$.

Figures 22 and 23 show the total deformation distribution of the PS and SS, respectively. Under both operating directions, the deformation of the blade gradually decreases from the LE to the TE. The deformation near the rim of the blade is larger than near the hub, and it is the largest at the rim of the LE. Because in order to avoid impeller cavitation in the design, the LE of the blade is thinned, leading to the LE being more sensitive to pressure changes.

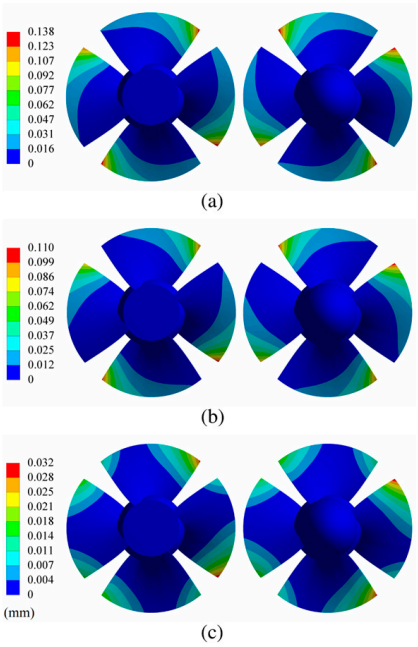


Figure 22. Total deformation of blades under forward operation: (**a**) $0.85Q_{f\,0}$ (from **left** to **right** is PS and SS, respectively), (**b**) $Q_{f\,0}$, (**c**) $1.20Q_{f\,0}$.

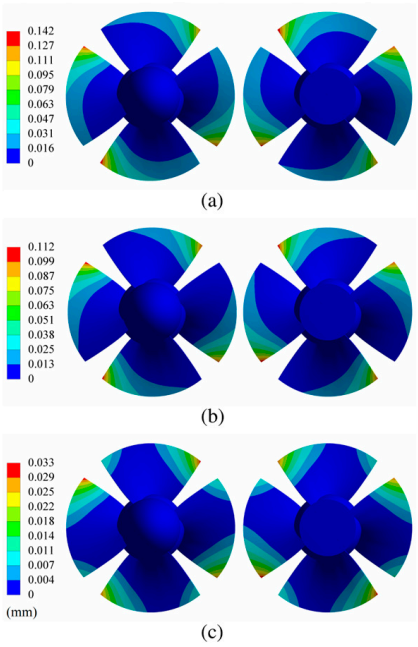


Figure 23. Total deformation of blades under reverse operation: (**a**) $0.85Q_{r0}$ (from **left** to **right** is PS and SS, respectively), (**b**) Q_{r0}, (**c**) $1.20Q_{r0}$.

With the increase in the flow rate, the maximum total deformation of the blade decreases, and the maximum total deformation in the low-flow-rate condition is 4.3 times than that in the large-flow-rate condition. The maximum total deformation is 0.138 mm under forward operation and 0.142 mm under the reverse operation. The total deformation is very small, which is also related to the fact that the pump is a model.

3.5. Cavitation

Cavitation causes noise and vibration, making the presence of cavitation in the pump detectable. This is manifested in the external characteristics as a rapid decline in efficiency. Figure 24 shows the comparison between computational and experimental results of the

vortex core region inside the impeller under forward operation. At the low flow rate, cavitation mainly occurs at the back of the LE and TE near the rim. Cavitation occurs at the LE near the rim and behind the TE at large flow rates. These two types of cavitation are primarily caused by the deviation of the operating condition from the design point, which causes the inlet velocity triangle to change, resulting in the flow separation on the PS or SS of the LE. To account for the performance under the reverse operation, Figure 11b shows that the flow state is not ideal at the design point. So, the vortex core region is similar to the low-flow condition, but the area is significantly reduced.

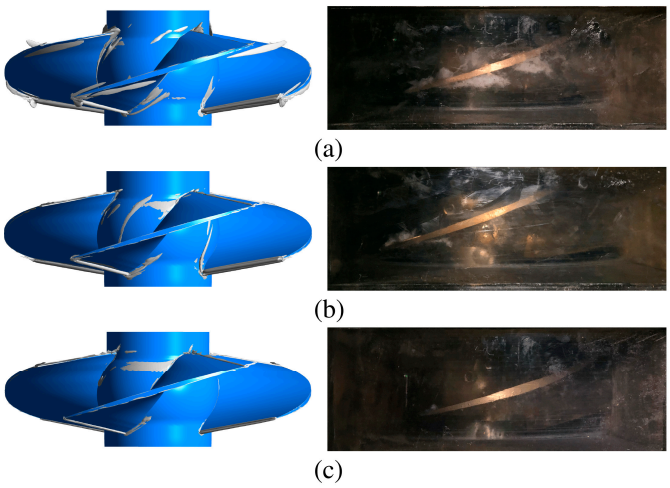


Figure 24. Comparison of computational (**left**) and experimental (**right**) vortex core region under forward operation: (**a**) $0.85Q_{f\,0}$, (**b**) $Q_{f\,0}$, (**c**) $1.20Q_{f\,0}$.

The vortex core region in the outlet passage under the reverse operation is shown in Figure 25. The circulation at the outlet of the impeller has a great impact under the reverse operation, so the vortex belt in the outlet passage exhibits strong rotation and obvious eccentricity under the low-flow condition. The circulation is small under the large-flow condition, so the vortex core region is small and extends in the direction of the rotating axis without eccentricity. Under the design condition, there is also a small eccentric vortex zone due to the lack of rectification effect of the rear guide vane.

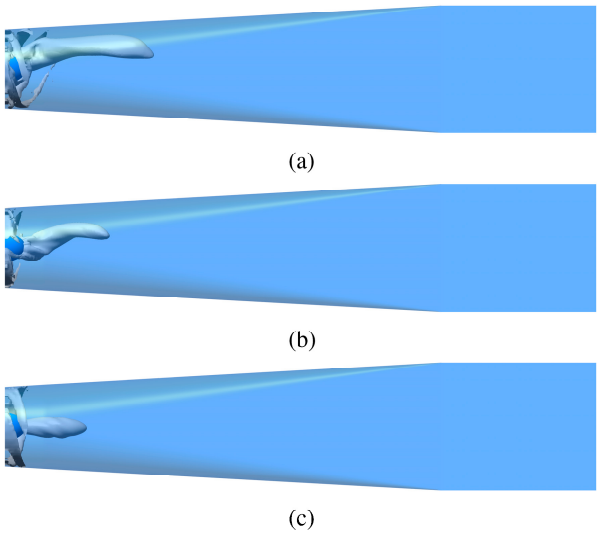


Figure 25. Vortex core region in the outlet passage under reverse operation: (**a**) $0.85Q_{r0}$, (**b**) Q_{r0}, (**c**) $1.20Q_{r0}$.

3.6. Pressure Fluctuation

The pressure fluctuation data under six operating conditions of point 1 and point 2 were obtained through experiments, where the maximum flow rate of $1.2Q_0$ is the near-zero head condition. As shown in Figure 26, the pressure fluctuation is analyzed with a 97% confidence level of the PTP value [28].

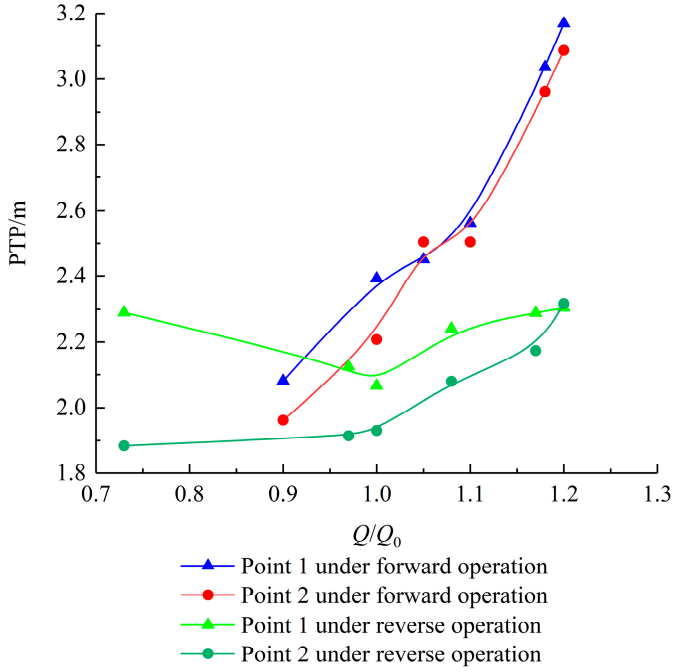


Figure 26. PTP values of pressure fluctuation.

Under the forward operation, the PTP value increases with the increase in flow rate and is the maximum at $1.2Q_{f\,0}$. The PTP value at point 1 is larger than that at point 2 under most of the conditions, indicating that the flow state has generally recovered after the redistribution of the guide vane and the adjustment of the S-shaped bend after transferring energy to the impeller. Under the reverse operation, the flow is smooth after passing through the tapered inlet passage. Then, after the pre-swirl in the guide vane and the rotating impeller, there is a large residual circulation at the outlet of the impeller, which causes the flow to be more turbulent (see Figure 10), and pressure fluctuation at point 1 increases as well. Due to the larger circulation, the gap between the two monitoring points is very large under the low-flow conditions. The difference is reduced as the flow rate increases and the circulation decreases.

In summary, after passing through the guide vane under forward operation, the circulation of the outlet passage has been greatly reduced. The pressure fluctuation is mainly influenced by the flow rate at this time, and the PTP value is the largest near the zero head. The circulation plays a dominant role in the influence of pressure fluctuation under re-verse operation, making the most dangerous operating conditions are low-flow conditions. So, the rectification effect of the guide vane has an obvious effect on the pressure fluctuation.

Fast Fourier transform (FFT) is performed on the time domain data to obtain the frequency domain results, as shown in Figure 27, where the horizontal coordinate is dimensionless by the rotational frequency, and the rotational frequency f_{n} = 906.67/60 = 15.11 Hz.

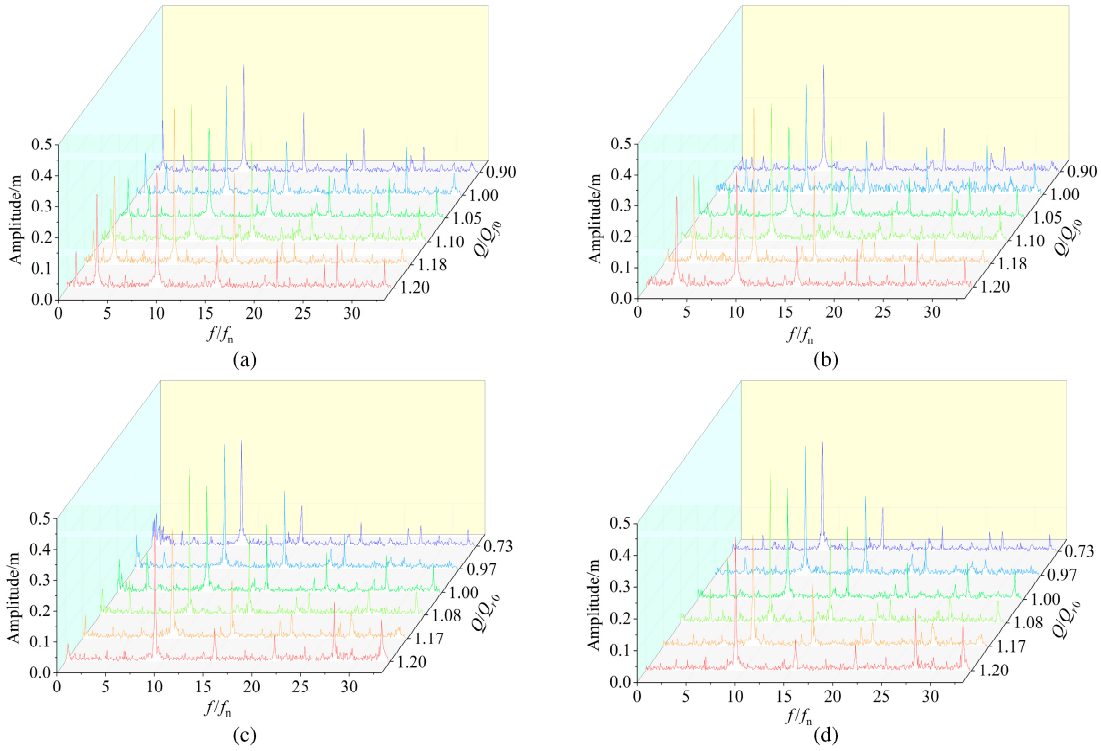


Figure 27. Frequency domain of pressure fluctuation: (**a**) point 1 under forward operation, (**b**) point 2 under forward operation, (**c**) point 1 under reverse operation, and (**d**) point 2 under reverse operation.

Under the forward operation, the PF of both points appears at f/f_n = 9.2, and the secondary frequency (SF) appears at f/f_n = 3.1 and 15.3. The maximum amplitudes of the two points under the same operating condition are almost the same, and the difference is within 2%. The maximum amplitude is the smallest at the design point and the largest near $1.2Q_{f\,0}$, i.e., near-zero head condition, and the maximum value is 1.8 times the minimum value. Under the reverse operation, the PF of both points appears at f/f_n = 9.2, and the SF appears at f/f_n = 15.3. The difference between the maximum magnitudes of the two points under the same operating condition is within 4%, and the maximum amplitude is the smallest at the design point. In particular, we notice that point 1 exhibits abnormal fluctuations at low frequencies, less than f_n under the reverse operation (see Figure 27c), and it is most noticeable at the minimum flow rate $0.73Q_{r0}$.

3.7. Vibration

Table 2 shows the PTP values of vibration acceleration and the position of PF in three directions under different operating conditions, where the PF is also dimensionless using the f_n. The experimental results show that the PTP values of the vibration acceleration in the vertical direction (*Z* direction) are the largest, indicating that the rotor system imbalance is one of the excitation sources causing the vibration. Because the impeller and rotating parts are inaccurate in geometry and material inhomogeneity during the manufacturing process. When the pump is running, it causes the rotor to become unbalanced, resulting in centrifugal inertia force and forced vibration of the pump device. Since the radial direction is constrained by two fixed supports, the PTP values of the vibration acceleration remain small overall.

Table 2. PF and PTP values (m/s^2) of acceleration of vibration.

Direction	Q/Q_0	X Direction		Y Direction		Z Direction	
		PTP Values	PF	PTP Values	PF	PTP Values	PF
Forward operation	1.20	0.742	3	0.732	3	1.665	3
	1.16	0.757	15	0.566	3	1.514	15
	1.10	0.723	9	0.625	4	1.870	4
	0.90	0.796	3	0.830	3	1.963	3
Reverse operation	1.20	0.645	3	0.615	3	1.533	3
	1.05	0.474	3	0.513	3	1.230	4
	0.97	0.547	3	0.581	4	1.475	1
	0.73	0.947	1	1.104	1	2.891	/

Note: / means no PF.

Under the forward operation, the maximum PTP values in all three directions occur at the low-flow condition of $0.90Q_{f\,0}$. On the one hand, there is an obvious back-flow area in the guide vane at this time (see Figure 11a), resulting in a high and low staggered distribution of velocity and pressure, thus causing vibration. On the other hand, there is obvious cavitation in the impeller (see Figure 24a), the highly elastic bubble attached to the blades, the bubble collapse, and rebound regeneration with the rotation of the impeller, which causes vibration. The PTP values are relatively large under the near-zero head condition. The vibration is due to the hydraulic vibration caused by the hydraulic imbalance and turbulent flow under the large-flow condition.

It can be seen from the frequency data that the PF of vibration is strongly related to the PSF of pressure fluctuation. It generally occurs at $3f_n$, $9f_n$, and $15f_n$, although at $1.10Q_{f\,0}$, the PF in the Y, Z directions occurs at the blade-passing frequency (BPF) $4f_n$. The vibration PF of the pump device changes with the flow rate and does not show obvious regularity, indicating that the reasons for vibration are complex, not only related to the system design but also related to the operating conditions. Therefore, it is necessary to give more attention and concern to this in practical engineering.

Under the reverse operation, the maximum PTP values in three directions also occurs at the minimum flow condition $0.73Q_{r0}$. On the one hand, the V_u and θ at the impeller inlet are very small under this condition, thus causing significant flow separation within the impeller (see Figure 14a). At the same time, due to the residual circulation at the impeller outlet being larger under the low-flow condition, an eccentric vortex belt forms in the outlet passage (see Figure 25a), which causes vibration. Under the near-zero head condition, a bigger vibration is caused by hydraulic vibration.

Under most operating conditions, the PF of vibration is the same as the PSF of pressure fluctuation, which is $3f_n$. However, $4f_n$ and f_n also appear in other operating conditions, and as the flow rate decreases, the PF in all directions decreases to f_n. On the one hand, the flow in the flow passage is more turbulent under low-flow conditions (see Figure 10a), which causes turbulent fluctuation and turbulent noise. On the other hand, the backflow vortex caused by the flow separation in the impeller and the outlet passage vortex caused by the circulation result in rapid enhancement of the low-frequency pressure fluctuation [1], which can also be seen in Figure 27c.

4. Conclusions

The flow characteristics, hydraulic loss, FSI, cavitation, pressure fluctuation, and vibration characteristics of an ultra-low-head bidirectional shaft extension pump, especially under near-zero head conditions, are investigated using theoretical analysis, numerical simulation, and experimental study. The following significant conclusions can be drawn:

Under the forward operation, a vortex is formed on the concave side of the S-shaped elbow under low-flow and design-flow conditions, and the closer the surface is to the shroud, the closer the vortex is to the back of the guide vanes, and the vortex area becomes smaller. Under the reverse operation, the vortex inside the outlet passage grows as the flow rate decreases. When the flow rate is less than $0.83Q_{r0}$, V_u and θ show an approximately exponential declining pattern.

Under the forward operation, the hydraulic loss of the outlet passage reaches the minimum value near the design point. The hydraulic loss of the outlet passage is 15% of the operating head at the minimum flow and 170% of the operating head under the near-zero head condition. Under reverse operation, the ratio of the local impact loss and vortex loss accounts for about 90% of the total hydraulic loss. The hydraulic loss of the outlet passage at the minimum flow rate is 61% of the operating head and 350% of the operating head under near-zero head condition. The R^2 for linear, power, and exponential fitting are 0.890, 0.963, and 0.978, respectively. So, the exponential fitting $y = 0.056e^{7.573x}$ can be better utilized for estimating the hydraulic loss of the outlet passage.

The equivalent stress decreases first and then increases from the LE to the TE under both operating directions. The larger equivalent stress appears near the rim of the LE and at the blade root near the LE. The deformation of the blade gradually decreases from the LE to the TE. The maximum total deformation in the low-flow-rate condition is 4.3 times that in the large-flow-rate condition. Under the forward operation, cavitation mainly occurs at the back of the LE and TE near the rim at low flow rates. Cavitation occurs at the LE near the rim and behind the TE at large flow rates. Under the reverse operation, the vortex belt in the outlet passage exhibits strong rotation and obvious eccentricity under the low-flow condition.

The pressure fluctuation is mainly influenced by the flow rate under the forward operation, and the PTP value is the largest near the zero head. The circulation plays a dominant role in the influence of pressure fluctuation under the reverse operation, making low-flow conditions the most dangerous operating conditions. The PF of vibration is strongly related to the PSF of pressure fluctuation, which generally occurs at $3f_{\mathrm{n}}$, $9f_{\mathrm{n}}$, and $15f_{\mathrm{n}}$ under the forward operation. Under the reverse operation, the PF of vibration occurs at $3f_{\mathrm{n}}$ under most conditions. $4f_{\mathrm{n}}$ and f_{n} also appear, and as the flow rate decreases, the PF decreases to f_{n}.

Author Contributions: All authors contributed to the study conception and design. Conceptualization and methodology are performed by Y.Z.; CFD simulations are performed by F.Z. and J.D.; experimental investigations are performed by F.Z. and G.L., writing—original draft preparation—is performed by F.Z.; writing—review and editing—is performed by F.Z. and Y.Z. All authors have read and agreed to the published version of the manuscript.

Funding: This work was funded by Ministry of Science and Technology of China (Grant No. 2019YFE0105200) and National Natural Science Foundation of China (Grant No. 51769035).

Data Availability Statement: The original contributions presented in this study are included in the article. Further inquiries can be directed to the corresponding author.

Conflicts of Interest: Authors Fulin Zhang and Gaohui Li were employed by the company PowerChina Huadong Engineering Corporation Limited. The remaining authors declare that the research was conducted in the absence of any commercial or financial relationships that could be construed as a potential conflict of interest.

References

1. Liu, C. *Pumps and Pumping Stations*; China Water & Power Press: Beijing, China, 2003.
2. Goltz, I.; Kosyna, G.; Stark, U.; Saathoff, H.; Bross, S. Stall inception phenomena in a single-stage axial-flow pump. *Proc. Inst. Mech. Eng. Part A J. Power Energy* **2003**, *217*, 471–479. [CrossRef]
3. Li, Y.; Wang, F. Numerical investigation of performance of an axial-flow pump with inducer. *J. Hydrodyn.* **2007**, *19*, 705–711. [CrossRef]
4. Zhang, D.; Shi, W.; Bin, C.; Guan, X. Unsteady flow analysis and experimental investigation of axial-flow pump. *J. Hydrodyn. Ser B* **2010**, *22*, 35–43. [CrossRef]
5. Prasad, V. Numerical simulation for flow characteristics of axial flow hydraulic turbine runner. *Energy Procedia* **2012**, *14*, 2060–2065. [CrossRef]
6. Kan, K.; Zheng, Y.; Chen, Y.; Xie, Z.; Yang, G.; Yang, C. Numerical study on the internal flow characteristics of an axial-flow pump under stall conditions. *J. Mech. Sci. Technol.* **2018**, *32*, 4683–4695. [CrossRef]
7. Yang, F.; Lin, Z.; Li, J.; Nasr, A.; Cong, W.; Li, C. Analysis of internal flow characteristics and structure optimization of vertical submersible axial flow pump device. *Adv. Mech. Eng.* **2022**, *14*, 1–23. [CrossRef]
8. Pozarlik, A.K.; Kok, J.B.W. Numerical investigation of one-and two-way fluid-structure interaction in combustion systems. In Proceedings of the International Conference on Computational Methods for Coupled Problems in Science and Engineering, Ibiza, Spain, 21 May–23 May 2007.
9. Benra, F.K.; Dohmen, H.J.; Pei, J.; Schuster, S.; Wan, B. A comparison of one-way and two-way coupling methods for numerical analysis of fluid-structure interactions. *J. Appl. Math.* **2011**, *2011*, 853560. [CrossRef]
10. Lerche, A.H.; Moore, J.J.; White, N.M.; Hardin, J. Dynamic stress prediction in centrifugal compressor blades using fluid structure interaction. *Turbo Expo Power Land Sea Air* **2012**, *44724*, 191–200.
11. Birajdar, R.; Keste, A. Prediction of flow-induced vibrations due to impeller hydraulic unbalance in vertical turbine pumps using one-way fluid- structure interaction. *J. Vib. Eng. Technol.* **2020**, *8*, 417–430. [CrossRef]
12. Shi, L.; Zhu, J.; Wang, L. Analysis of Strength and Modal Characteristics of a Full Tubular Pump Impeller Based on Fluid-Structure Interaction. *Res. Sq.* **2021**. [CrossRef]
13. Zhang, D.; Shi, W.; Van Esch BP, M.B.; Shi, L.; Dubuisson, M. Numerical and experimental investigation of tip leakage vortex trajectory and dynamics in an axial flow pump. *Comput. Fluids* **2015**, *112*, 61–71. [CrossRef]
14. Zhang, D.; Shi, W.; Pan, D.; Dubuisson, M. Numerical and experimental investigation of tip leakage vortex cavitation patterns and mechanisms in an axial flow pump. *J. Fluids Eng.* **2015**, *137*, 121103. [CrossRef]
15. Feng, H.; Wan, Y.; Fan, Z. Numerical investigation of turbulent cavitating flow in an axial flow pump using a new transport-based model. *J. Mech. Sci. Technol.* **2020**, *34*, 745–756. [CrossRef]
16. Wang, C.; Wu, S.; Shi, W.; Yao, J. Numerical calculation and experimental research of pressure fluctuation in the pump under different operating conditions. *J. Vibroeng.* **2013**, *15*, 2049–2056.
17. Ma, P.; Wang, J.; Li, H. Numerical analysis of pressure pulsation for a bidirectional pump under positive and reverse operation. *Adv. Mech. Eng.* **2014**, *6*, 730280. [CrossRef]
18. Xie, C.; Tang, F.; Zhang, R.; Zhou, W.; Zhang, W.; Yang, F. Numerical calculation of axial-flow pump's pressure fluctuation and model test analysis. *Adv. Mech. Eng.* **2018**, *10*, 1687814018769775. [CrossRef]
19. Shervani-Tabar, M.T.; Ettefagh, M.M.; Lotfan, S.; Safarzadeh, H. Cavitation intensity monitoring in an axial flow pump based on vibration signals using multi-class support vector machine. *Proc. Inst. Mech. Eng. Part C J. Mech. Eng. Sci.* **2018**, *232*, 3013–3026. [CrossRef]
20. Menter, F.R. Review of the shear-stress transport turbulence model experience from an industrial perspective. *J. Comput. Fluid Dyn.* **2009**, *23*, 305–316. [CrossRef]
21. Feng, W.; Cheng, Q.; Guo, Z.; Qian, Z. Simulation of cavitation performance of an axial flow pump with inlet guide vanes. *Adv. Mech. Eng.* **2016**, *8*, 1687814016651583. [CrossRef]
22. Shi, W.; Wang, C.; Wang, W.; Pei, B. Numerical calculation on cavitation pressure pulsation in centrifugal pump. *Adv. Mech. Eng.* **2014**, *6*, 367631. [CrossRef]
23. Marsh, P.; Ranmuthugala, D.; Penesis, I.; Thomas, G. Numerical investigation of the influence of blade helicity on the performance characteristics of vertical axis tidal turbines. *Renew. Energy* **2015**, *81*, 926–935. [CrossRef]
24. Tan, L.; Zhu, B.; Wang, Y.; Shuliang, C.; Gui, S. Numerical study on characteristics of unsteady flow in a centrifugal pump volute at partial load condition. *Eng. Comput.* **2015**, *32*, 1549–1566. [CrossRef]
25. Zheng, Y.; Li, P.; Chen, X.; Wang, C. Hydraulic design on circulation pipe system for hydraulic machinery multifunctional model test bench. *Fluid Mach.* **2001**, *29*, 16–18.
26. Lu, L. *Optimized Hydraulic Design of High Performance Large Low Head Pump Units*; China Water & Power Press: Beijing, China, 2013; Volume 91.

27. Zhang, R.; Chen, H. *Numerical Simulation and Flow Diagnosis of Axial-Flow Pump at Part-Load Condition*; De Gruyter: Berlin, Germany, 2012; Volume 29, pp. 1–7.
28. Zhang, D.; Geng, L.; Shi, W. Experimental investigation on pressure fluctuation and vibration in axial-flow pump model. *Nongye Jixie Xuebao/Trans. Chin. Soc. Agric. Mach.* **2015**, *46*, 66–72.

Disclaimer/Publisher's Note: The statements, opinions and data contained in all publications are solely those of the individual author(s) and contributor(s) and not of MDPI and/or the editor(s). MDPI and/or the editor(s) disclaim responsibility for any injury to people or property resulting from any ideas, methods, instructions or products referred to in the content.